Research Square

Preprints are preliminary reports that have not undergone peer review.
They should not be considered conclusive, used to inform clinical practice,
or referenced by the media as validated information.

Ch25h/25HC axis orchestrates phagocytosis and lipid metabolism after intracerebral haemorrhage

Catherine B. Lawrence

Catherine.Lawrence@manchester.ac.uk

University of Manchester, Division of Neuroscience and Experimental Psychology, and Geoffrey Jefferson Brain Research Centre, Faculty of Biology, Medicine and Health, Manchester Academic Health Scie https://orcid.org/0000-0002-2372-2968

Ran Zhou

University of Manchester

Victor Tapia

University of Manchester https://orcid.org/0000-0001-5009-4779

Abigail Bennington

University of Manchester

Ruyue Gao

University of Manchester

Milo Elmes

University of Manchester

I-Hsuan Lin

University of Manchester https://orcid.org/0000-0002-6207-1299

Ziyu Dai

Sun Yat-Sen University Cancer Center

Siohban Crilly

University of Manchester

Caroline Pot

Lausanne University Hospital and University of Lausanne

Stuart Allan

University of Manchester

Paul Kasher

University of Manchester

Article

Keywords: intracerebral haemorrhage, Ch25h, 25HC, phagocytosis, lipid metabolism

Posted Date: February 20th, 2026

DOI: https://doi.org/10.21203/rs.3.rs-8845215/v1

License: This work is licensed under a Creative Commons Attribution 4.0 International License.
Read Full License

Additional Declarations: There is **NO** Competing Interest.

Abstract

Intracerebral haemorrhage (ICH) is a devastating form of stroke for which therapies are lacking. Secondary brain injury driven by erythrocyte lysis contributes to poor outcomes, highlighting the need to enhance endogenous haematoma clearance. Here, we identify cholesterol 25-hydroxylase (CH25H) and its product 25-hydroxycholesterol (25HC) as key regulators of phagocytic and lipid-handling responses after ICH. CH25H expression was increased in postmortem human ICH tissue and a mouse ICH model, localising predominantly in perihaematomal phagocytes. Ch25h deficiency in mice exacerbated blood-brain barrier disruption, iron deposition, and neurological deficits after ICH. Conversely, 25HC treatment improved functional recovery and reduced tissue pathology. Single-cell RNA sequencing revealed selective upregulation of Ch25h in activated microglia after ICH, which modulated phago-lysosomal and lipid metabolic gene expression. Consistently, 25HC enhanced erythrocyte phagocytosis and limited lipid droplet accumulation in vitro. Together, these findings identify CH25H/25HC-dependent lipid reprogramming as a critical determinant of phagocyte function and neurological recovery after ICH.

Introduction

Intracerebral haemorrhage (ICH) is the deadliest type of stroke with nearly 50% mortality that accounts for almost 6% of all global deaths, with those who survive frequently being left with life-changing impairments[1]. Unlike ischaemic stroke, which has benefitted from therapeutic advancements including thrombolysis and mechanical thrombectomy, there are currently no reliably effective treatment options for ICH, so there is an urgent need for new therapies to improve patient survival and quality of life.

ICH-induced brain injury results from the initial physical mass effect of the haematoma and subsequent secondary injury induced by erythrocyte lysis. Erythrocyte lysis releases haemoglobin, which breaks down into haem/haemin and free iron, and also generates thrombin, all of which are pro-inflammatory and directly toxic to neurones and glia[2]. Fast and efficient resolution of the haematoma is therefore key to limiting the toxic actions of the extravasated blood and reducing mass effect from the haematoma. Surgical removal of the haematoma reduces mortality in patients, but so far has failed to improve neurological outcome due to an inability to clear all the haematoma[3]. Natural haematoma resolution occurs over days, weeks to months after ICH in patients[4]. As this endogenous process takes time and is often incomplete, discovering new ways to enhance haematoma clearance could markedly improve outcome after ICH.

Microglia and monocyte-derived macrophages (MDMs) are innate immune cells that contribute to neuroinflammation and worsen outcome after ICH due to their pro-inflammatory capacity. However, both cell types exhibit functional plasticity and, as professional phagocytes, can play a reparative role in haematoma clearance through phagocytosis of erythrocytes, their breakdown products and cellular debris[2]. In experimental ICH, enhancing the reparative role of MDMs reduces haematoma volume and improves outcome[5,6]. MDMs have a higher phagocytic activity for erythrocytes after ICH compared to brain resident microglia[7]. However, MDMs require access to the brain and account for less than 10% of

immune cells seen in ICH, whereas microglia are brain resident and are highly abundant in ICH (making up to 70% of immune cells). Thus, finding a way to stimulate the phagocytic capacity of microglia (and MDMs) could significantly enhance haematoma clearance after ICH and improve outcome.

Ch25h is an interferon (IFN)-stimulated gene encoding an enzyme that catalyses the conversion of cholesterol into the oxysterol 25-hydroxycholesterol (25HC). While Ch25h plays a key role in cholesterol metabolism, emerging evidence suggests that it, and its product 25-HC, can also regulate inflammatory responses[8-10]. In the healthy brain, *Ch25h* is expressed at low levels in border-associated macrophages[11] and endothelial cell populations[12,13]. *Ch25h* expression is elevated in several neurological conditions, where it modulates neuroinflammation, including Alzheimer's disease[14-16], X-linked adrenoleukodystrophy[17], autoimmune encephalomyelitis[18], and ischaemic stroke[19]. Furthermore, exogenous 25HC treatment after experimental ischaemic stroke reduces infarct volume and neurological deficits[20], suggesting a protective role for Ch25h through 25HC in ischaemic stroke. Although the mechanisms underlying this protective effect remain unclear, recent data indicate that microglia expressing Ch25h exhibit increased phagocytosis and improve outcome after ischaemic stroke[19]. Consistent with this, a role for Ch25h in phagocytosis has also been proposed in peripheral myeloid cells as this enzyme and 25HC are needed for efficient phagocytosis by peripheral macrophage cells[21,22].

Here, we investigated the role of the Ch25h/25HC axis in ICH and tested the hypothesis that Ch25h promotes erythrocyte clearance by microglia and MDMs, and can thus limit secondary injury after ICH. Using a combination of human tissue analysis, a mouse model of ICH, single-cell transcriptomics, and *in vitro* assays, we demonstrate that *Ch25h* is selectively induced in activated microglial populations after ICH. Genetic loss of *Ch25h* exacerbated pathological and functional outcomes after ICH, whereas treatment with 25HC improved recovery. Moreover, single-cell transcriptomic and *in vitro* analyses showed that 25HC modulated phagocytic and lipid-handling responses in microglia and macrophages, linking Ch25h activity to coordinated clearance of red blood cells (RBC) and the associated lipid burden.

Results

Ch25h expression increases after intracerebral haemorrhage

The expression of CH25H was examined in post-mortem brain tissue from patients after ICH (Fig. 1a). No CH25H staining was detected in control brains whereas a small number of CH25H-positive cells were observed in the brains of ICH patients at acute (2-3 days) time points, with a marked increase in the number of CH25H-positive cells at chronic time points (2-8 months),
particularly surrounding the haemorrhage site. Quantification confirmed a significantly higher area covered by CH25H-positive cells in the chronic ICH brains, compared to controls (Fig. 1b).

To assess whether this response was recapitulated in experimental ICH, we next examined Ch25h expression in a mouse model of collagenase-induced ICH. Ch25h-positive cells were detected within the

haemorrhagic core at 6 h, 1 day, and 3 days post-injury with a progressive increase over time, while being absent in the contralateral (non-haemorrhagic) region (Fig. 1c). Quantitative analysis revealed a significant increase in the area covered by cells positive for Ch25h at all time points (Fig. 1d). *Ch25h* mRNA expression was also increased in the haemorrhage area from 1-7 days after ICH in mice when compared to the contralateral region, reaching peak expression at day 3 post-ICH (approximately 15-fold higher than contralateral tissue) (Fig. 1e). Given the presence of Ch25h-positive cells in the lesion and its previously described role in phagocytes[19,21,22], we investigated their identity using Iba1 as a marker of microglia/macrophages. Dual immunofluorescence at 3 days post-ICH in mice confirmed that Ch25h was expressed in Iba1-positive cells displaying a morphology consistent with phagocytic cells, including enlarged cell bodies and intracellular vacuole-like structures, which were frequently associated with residual RBCs (Fig. 1f). As previously observed by immunohistochemistry, no Ch25h immunofluorescence was detected in the contralateral region (Fig. S1).

To investigate the mechanism underlying *Ch25h* upregulation, BV2 microglial cells and primary bone-marrow derived macrophages (BMDMs) were exposed to two *in vitro* ICH models: haemin exposure or induction of RBC phagocytosis. Haemin stimulation (100 μM, 6 h) significantly increased *Ch25h* expression by approximately two-fold in BV2 microglia and markedly in BMDMs (~45-fold) (Fig. 1g,h), without evidence of cytotoxicity (Fig. S2a,b). Phagocytosis of IgG-opsonised RBCs was validated by a pHrodo-based phagocytosis assay (Fig. S2c,d). *Ch25h* was significantly upregulated by 2.5-fold in BV2 microglia 6 h after phagocytosis was initiated (Fig. 1i), with only a modest, non-significant increase observed in BMDMs under the same conditions (Fig. 1j).

Ch25h deficiency leads to worse outcome after ICH

Having established that *Ch25h* is robustly induced following ICH, we next examined whether *Ch25h* deficiency influences outcomes in the collagenase-induced ICH mouse model. We first determined whether Ch25h modulated the initial primary haemorrhage severity in male and female *Ch25h* deficient (*Ch25h*$^{-/-}$)[23] and wild-type (*Ch25h*$^{+/+}$) mice. No significant differences in haematoma volume were observed between genotypes or sexes at 24 h (Fig. 2a) and 3 days post-ICH (Fig. 2b). Given the absence of sex differences, subsequent analyses focused on mixed-sex cohorts, unless stated otherwise. Despite similar haematoma volumes, by 3 days post-ICH *Ch25h*$^{-/-}$ mice exhibited significantly increased brain-blood barrier (BBB) permeability, with an 80% increase in IgG extravasation (Fig. 2c) and elevated iron deposition, increased by 150% compared to *Ch25h*$^{+/+}$ wild-type mice (Fig. 2d). These pathological changes were associated with greater ICH-induced weight loss in *Ch25h*$^{-/-}$ mice, with significantly increased weight loss observed at days 2-4 days post-ICH, and peaking at day 2 (Fig. 2e). Consistent with these findings, neurological function, assessed by a composite neurological deficit score, revealed a significant effect of time ($p < 0.0001$), with performance declining from baseline in both genotypes ($p < 0.0001$). However, *Ch25h*$^{-/-}$ mice displayed significantly more severe deficits at days 1, 3 and 7 compared to *Ch25h*$^{+/+}$ mice (Fig. 2f). In the cylinder test, use of the impaired limb was significantly reduced in both genotypes following ICH ($P<0.001$, significant effect of time), but this reduction was significantly more

pronounced in *Ch25h*$^{-/-}$ mice on day 1 (Fig. 2g). To further assess general wellbeing, the nest-building test was performed. Although there was no significant overall effect of time (P = 0.057), *Ch25h*$^{-/-}$ mice demonstrated poorer nest-building performance compared to *Ch25h*$^{+/+}$ mice at day 1 post-ICH (Fig. 2h).

25HC improves outcome after ICH

As *Ch25h* deficiency worsened outcome after ICH in mice, we next tested the hypothesis that its enzymatic product 25HC may have therapeutic potential to improve outcome following ICH. To determine whether peripherally administered 25HC could elicit molecular responses within the haemorrhage, we measured the expression of 25HC-responsive genes in contralateral and ipsilateral tissue. 25HC and other endogenous oxysterols activate Liver X receptor (LXR) transcription factors[24]. Although the precise binding of 25HC has not been experimentally elucidated, molecular docking analysis predicted that 25HC binds to the ligand-binding domain of LXRs (Fig. S3) in a similar manner to other ligands[25,26]. In parallel, 25HC inhibits the Sterol Regulatory Element-Binding Protein 2 (SREBP2) transcription factor by binding at the interface of a regulatory protein complex that controls SREBP2 trafficking[27,28]. A single intraperitoneal injection of 25HC (50 mg kg^{-1}) after ICH induction significantly increased expression of the LXR targets *Abca1* and *Abcg1*, and reduced the expression of the SREBP2 target *Hmgcr*, in the haemorrhagic brain tissue at 24 h post-ICH (Fig. 3a). Together, these data indicate that peripheral 25HC administration modulates transcriptional responses in the haematoma consistent with engagement of established 25HC targets.

In addition to modulating LXR and SREBP2 targets, 25HC treatment significantly reduced the expression of inflammatory mediators *Il1b* and *Mmp9* in the haemorrhagic brain tissue, while increasing, in a non-significant manner, expression of the scavenger receptor *Cd36* (Fig. 3a). These transcriptional changes were associated with improved neurological scores at 24 h post-ICH, without affecting weight loss (Fig. S4). We next evaluated whether these beneficial effects were sustained when animals received daily intraperitoneal 25HC injections for 3 days starting immediately after ICH induction. 25HC treatment did not affect haematoma volume at day 3 (Fig. 3b), but it was associated with a marked reduction in BBB permeability (~66% reduction) and a significant decrease in iron deposition at the haematoma border (~63% reduction) (Fig. 3c,d). These effects were accompanied by significantly attenuated weight loss, improved neurological scores, and enhanced grip strength at day 3 post-ICH, collectively indicating that 25HC improves functional recovery following ICH (Fig. 3e-g).

Ch25h is upregulated in activated microglial populations after ICH

Given the effects of *Ch25h* deficiency and 25HC treatment on ICH outcomes, we next investigated how this pathway shapes cellular responses in the injured brain. We performed single-cell RNA sequencing on mouse brain tissue collected 3 days after ICH. Conditions included contralateral hemispheres (defined as Control) and ipsilateral hemispheres from *Ch25h*$^{+/+}$ mice (defined as ICH), as well as ipsilateral tissue from *Ch25h*$^{-/-}$ mice (ICH *Ch25h*$^{-/-}$) and 25HC-treated *Ch25h*$^{+/+}$ mice (ICH 25HC) (Fig.

4a). Clustering identified major coarse cell populations present across conditions (Fig. S5a,b). When control and ICH conditions were analysed together to assess coarse cell type-specific expression patterns, *Ch25h* expression was predominantly localised to microglial, macrophage and endothelial populations (Fig. 4b), while it was barely detected in neuronal, glial, epithelial or fibroblast cell types (Fig. S5b,c). In contrast, comparison of Control and ICH conditions revealed a marked increase in the proportion of *Ch25h*-expressing microglia and a modest increase in macrophages in response to ICH (Fig. 4c, S5b-d). Pseudo-bulk differential expression analysis further confirmed significant upregulation of *Ch25h* selectively in microglia following ICH, with no significant changes detected in endothelial cells or macrophages (Table S1).

To examine cell heterogeneity in more detail, cells were further subclustered using an unsupervised approach across all conditions and subsequently annotated by selected gene markers, and pairwise comparisons were made between all conditions (Fig. 4a). Three microglial (Fig. 4d), four macrophage and one monocyte clusters were detected (Fig. S6a-b). Microglial clusters were annotated as homeostatic (expressing *P2ry12*, *Tmem119*, and *Siglech*), inflammatory (characterised by reduced expression of homeostatic markers), and disease-associated microglia, defined by high expression of *Spp1*, *Hmox1*, *Msr1*, and *Lilrb4a* (Fig. S6a). These annotations were validated by comparing the activity of previously described microglial transcriptional activation states within these clusters[19,29,30]. The inflammatory cluster was primarily associated with an injury-responsive microglia (IRM) gene signature, whereas the cluster annotated here as disease-associated microglia showed activity of both IRM and the previously defined disease-associated microglia (DAM) transcriptional signature (Fig. S6c). Both inflammatory and disease-associated microglia clusters expanded in number after ICH (Fig. 4e), and a high number of *Ch25h*-expressing cells were found in these activated states (Fig. 4f). *Ch25h* was among the top upregulated genes in inflammatory microglia in response to ICH (Table S2), while changes in homeostatic microglia were minimal despite reaching statistical significance (Table S3). Differential expression in disease-associated microglia could not be estimated in response to ICH due to the absence of this population in the control condition (Fig. 4e). Border-associated macrophage, infiltrating macrophages and monocyte clusters were also annotated (Fig. S6a,b,d), but a lower proportion of *Ch25h*-expressing cells was observed in these clusters, and no significant upregulation was detected by pseudo-bulk analysis (Fig. S6e, Table S3).

Ch25h/25HC pathway modulates a phago-lysosomal program after ICH

Given the strong induction of *Ch25h* in inflammatory microglia following ICH, we next characterised the ICH-induced transcriptional response of this cluster. Over-representation analysis of significantly upregulated genes in response to ICH (n = 381, FDR < 0.05; $\log_2$FC > 1) showed enrichment of KEGG pathways related to lysosomal function, phagocytosis and efferocytosis (Fig. 4g, Table S4), consistent with a phagocytic phenotype. This enrichment was specific to inflammatory microglia, as homeostatic microglia did not show a similar pathway representation in genes upregulated in response to ICH (Table S5). Gene set enrichment analysis (GSEA) independently confirmed positive enrichment of these pathways in inflammatory microglia (Fig. 4h, Table S6). To assess whether *Ch25h* and 25HC modulate

these transcriptional programmes, we then compared the ICH *Ch25h*$^{+/+}$ condition with ICH *Ch25h*$^{-/-}$ (*Ch25h* deficiency comparison) or with 25HC-treated *Ch25h*$^{+/+}$ (25HC treatment comparison) (Fig 4a). As these comparisons yielded few or no significant differentially expressed genes (FDR > 0.05) in microglial and macrophage clusters (Table S7), enrichment analyses were restricted to GSEA. Both *Ch25h*-deficient and 25HC treatment conditions showed negative enrichment of KEGG lysosome and phagosome pathways in the inflammatory microglia cluster (Fig. 4i), with these terms ranked among the top five enriched pathways in each comparison. The core gene sets driving these enrichments showed only modest overlap (Fig. 4j), suggesting that *Ch25h*-deficiency and 25HC treatment influenced distinct components of the phago-lysosomal pathway. Interestingly, negative enrichment of phagosome and lysosome KEGG pathways in the 25HC-treated comparison was also observed in disease-associated microglia and the macrophage cluster annotated as inflammatory macrophages (Fig. 4k). Pathway analysis revealed that disease-associated microglia and inflammatory macrophages showed the highest phago-lysosomal activity compared with other clusters (Fig. S7a,b), suggesting that 25HC treatment modulates the activity of several phagocytic myeloid cell types in the haemorrhagic tissue.

Together, these data indicate that *Ch25h* is upregulated after ICH in an inflammatory microglia subcluster alongside upregulation of a phagocytosis programme. *Ch25h* deficiency alters the phagocytic signature of this microglial cluster, whereas 25HC treatment modulates phago-lysosomal pathways across multiple microglial and macrophage populations responding to ICH.

25HC promotes RBC phagocytosis and lipid handling

To functionally validate the role of 25HC in phagocytosis, we examined its effects in *in vitro* assays. BMDMs pre-treated with 25HC (1 μM, 24 h) exhibited significantly enhanced phagocytosis of both oxidised and IgG-opsonised RBCs in a pHrodo-based phagocytosis assay (Fig. 5a-d). This increase in phagocytosis was not due to alterations in cell density or cytotoxicity but was accompanied by a modest increase in cell area (Fig. S8a-c). A similar modulatory effect was observed in BV2 microglia. While BV2 microglia pre-treated with 25HC (1 μM, 24 h) showed no change in RBC phagocytosis (Fig. S8d), extending the treatment to include incubation during phagocytosis resulted in a significant increase (Fig. 5e).

To explore the mechanisms underlying these effects, we performed bulk RNA sequencing on BMDMs pre-treated with 25HC for 24 h and subsequently exposed to opsonised RBCs for 24 h (Fig. 5f). Genes differentially regulated (FDR<0.05) in opposite directions by RBC phagocytosis or 25HC were analysed by pathway enrichment analysis (Fig. 5g). Among genes upregulated by RBC phagocytosis and downregulated by 25HC (n=141 genes, Table S8), phagocytosis- and lipid-related pathways were identified in both Gene Ontology (GO) and KEGG databases (Fig. 5h, Fig. S8a, Table S9,10). In contrast, the 39 genes (Table S8) downregulated by RBC phagocytosis and upregulated by 25HC did not yield significant pathway enrichment. A second analysis using an interaction model identified 31 genes with a differential response to RBC phagocytosis in the presence of 25HC pre-treatment (Fig. S9b,c, Table S11), which were also enriched for cholesterol and lipoprotein-related GO terms (Fig. S9d, Table S12).

These results suggest that RBC phagocytosis induces cholesterol metabolic reprogramming in macrophages, which is modulated by 25HC. To assess whether similar regulation occurred *in vivo*, we examined the GSEA results from our single-cell dataset (Fig. 4a). In response to ICH, microglial and macrophage clusters showed positive enrichment of the cholesterol metabolism KEGG pathway (Fig. 5i). On the contrary, 25HC-treatment negatively enriched the cholesterol metabolism KEGG pathway (Fig. 5i), particularly in the same microglial and macrophage clusters that showed a phago-lysosomal modulation (Fig. 4k). Related GO terms such as response to lipoprotein particle and sterol processes were also negatively enriched by *Ch25h*-deficiency in microglial clusters (Fig. S9e). To evaluate changes in lipid metabolism during RBC clearance, and given the established role of *Ch25h* in the regulation of neutral lipid handling during efferocytosis[22], we quantified lipid droplets (LDs) in BMDMs after 25HC pre-treatment and RBC phagocytosis. Exposure to RBCs increased LD accumulation, whereas 25HC pre-treatment attenuated this lipid loading (Fig. 5j,k). Collectively, these data identify a role for Ch25h and 25HC coordinating phagocytosis and lipid metabolic responses in microglia and macrophages after ICH.

Discussion

Here, we report a robust upregulation of Ch25h in response to ICH using multiple approaches, including analysis of post-mortem human brain samples, an experimental mouse model, and *in vitro* models of RBC phagocytosis and haemin exposure. Functional evaluation of *Ch25h* deficiency and 25HC treatment in mouse ICH demonstrated that the Ch25h/25HC axis improves recovery after ICH, including outcomes related to BBB disruption, ferric iron deposition, and behaviour. Importantly, CH25H was chronically expressed in the post-ICH human brain, indicating that this axis is an active endogenous response in patients and therefore a potential translational target to improve clinical outcomes.

Mechanistically, our data demonstrate that *Ch25h* upregulation is associated with modulation of phagocytic activity in microglia. Ch25h was detected in Iba1-positive cells with phagocytic morphology in mouse ICH, which were subsequently identified by scRNA-seq as activated microglia states. *Ch25h* was upregulated alongside phagosome and lysosome pathways in inflammatory microglia following ICH, and both *Ch25h* deficiency and 25HC treatment modulated this transcriptional programme during ICH. This transcriptional regulation was associated with reduced ferric iron deposition following 25HC treatment and increased iron accumulation in *Ch25h*-deficient mice, consistent with the established link between iron handling and RBC clearance by phagocytes in the brain and other tissues[31-33]. *In vitro* models further supported this association, as BV2 microglia significantly upregulated *Ch25h* in response to RBC phagocytosis and haemin exposure, and 25HC treatment enhanced BV2 RBC phagocytosis.

In contrast to microglia, *Ch25h* upregulation in BMDMs was observed only following haemin exposure *in vitro* and was not significant during RBC phagocytosis, or in macrophages identified by scRNA-seq in response to ICH. Nevertheless, 25HC treatment modulated the expression of phagosome and lysosome pathways in inflammatory macrophages during ICH and promoted RBC phagocytosis by BMDMs *in vitro*.

Together, these findings indicate that while *Ch25h* is endogenously activated in microglia following ICH, exogenous 25HC can enhance RBC clearance in both microglia and macrophages. These observations closely align with previous work supporting a role of *Ch25h* and 25HC in promoting phagocytosis, as observed in microglia[19] and in peripheral macrophages[21,22]. Extending these findings to ICH is particularly important given the central role of haematoma clearance by microglia and macrophages in limiting secondary brain injury following haemorrhage[6,34,35].

Our results suggest that the Ch25h/25HC axis influences phagocytosis through the modulation of lipid handling. In response to ICH, microglia and macrophage clusters positively showed upregulation of cholesterol metabolism, whereas 25HC treatment induced the opposite regulatory pattern. Similar effects were observed in bulk RNA-seq analysis of BMDMs following RBC phagocytosis and 25HC treatment. Importantly, in response to RBC phagocytosis, BMDMs exhibited increased LD accumulation, and this response was significantly attenuated by 25HC treatment. This is consistent with previous reports showing increased neutral lipid accumulation in *Ch25h*-deficient efferocytic alveolar macrophages[22], elevated LD content in BMDMs after *Ch25h* siRNA knock-down[36], and reduced *Ch25h* expression in LD-rich microglia[37]. Our observation that 25HC modulates LD accumulation during RBC clearance is especially relevant given the critical role of LD biology in brain pathology. LDs are scarce in the healthy brain but accumulate with ageing, Alzheimer's disease and ischaemic stroke, where persistent microglial lipid loading is associated with impaired phagocytosis and pro-inflammatory phenotypes[37-39]. Notably, LD accumulation has been reported at chronic stages up to 28 days after mouse ICH[40], and pharmacological modulation of LDs has been shown to improve neurological outcomes after ICH[41,42]. Although most of our analyses focused on the early phase after ICH, CH25H was detected in chronic human ICH samples, and *Ch25h* upregulation in mice persisted for at least 7 days post-injury. This suggests that sustained activation of the CH25H/25HC axis may contribute to longer-term modulation of lipid handling, microglial function and recovery following ICH.

Future steps should identify how 25HC modulates RBC phagocytosis and lipid handling. Extensive work in infection models has demonstrated that 25HC remodels multiple pathways to restrict cholesterol availability as a defence mechanism. This includes inhibition of SREBP2-driven cholesterol synthesis, cholesterol internalisation by activation of Acyl-CoA:cholesterol acyltransferase (ACAT), and cholesterol efflux through activation of LXR signalling[28,43-45]. By contrast, how modulation of these pathways influences phagocytosis is less well understood. Among the pathways regulated by 25HC, LXR signalling represents a particularly compelling candidate mechanism. LXR activation is known to promote efferocytosis by inducing the expression of phagocytic receptors and facilitating lipid handling after cargo degradation[46,47]. Supporting the relevance of this pathway *in vivo*, we detected a significant upregulation of LXR-targets *Abca1* and *Abcg1*, two proteins involved in cholesterol efflux in the brain[48,49], in the haematoma area after 25HC treatment, and direct LXR activation has previously been shown to reduce LD burden and improve outcomes after ICH[42]. The contribution of the other 25HC-modulated pathways is less clear. Activation of SREBP2 has been proposed to promote phagocytosis by supporting

membrane biogenesis[50], and consistent with this, BMDMs upregulated cholesterol synthesis genes in response to RBC phagocytosis. Notably, this response was inhibited by 25HC treatment, suggesting that the enhanced RBC phagocytosis observed *in vitro* does not require increased endogenous cholesterol synthesis. In addition, 25HC has been reported to promote LD formation through ACAT-mediated cholesterol esterification[43,51]. This appears at odds with our findings showing reduced LD accumulation following 25HC treatment. These observations highlight the need for a more detailed understanding of how cholesterol synthesis, efflux, and LD dynamics are coordinated by 25HC during haematoma clearance.

Another possible mechanism of phagocytosis regulation highlighted by the scRNA-Seq analysis is the lysosome pathway. A link between the Ch25h/25HC axis and lysosomal biology has recently been described. In macrophages, 25HC has been shown to accumulate within lysosomes, activate AMPK (5' adenosine monophosphate-activated protein kinase) signalling, and induce broad immune and metabolic changes[52]. However, whether 25HC directly modulates lysosomal dynamics during phagocytosis, for example by promoting phagolysosome formation or maturation[53], remains unknown. Interestingly, lysosomal dysfunction has been reported to upregulate *Ch25h* expression and increase 25HC production in pulmonary endothelial cells[54], suggesting the existence of a feedback loop linking lysosomal stress to *Ch25h* induction.

In summary, this study identifies the Ch25h/25HC axis as an endogenous regulator of phagocytic and metabolic responses after ICH, linking RBC clearance to coordinated phago-lysosomal and lipid-handling pathways in microglia and macrophages. By demonstrating that exogenous 25HC improves ICH outcomes, our findings highlight the Ch25h/25HC axis as a therapeutic target for enhancing RBC phagocytosis, lipid handling and improving recovery. Defining the downstream metabolic and phagocytic pathways activated by 25HC will be a critical next step to enable targeted intervention and translation of these findings toward effective therapies for ICH.

Methods

Human samples

Human post-mortem brain tissue was obtained from the Edinburgh Brain Bank, University of Edinburgh, UK. Tissue was donated from a cohort of mixed sex patients (age 63-86) who died after a deep (basal ganglia or thalamus) ICH at acute (n=3 at 2-3 days) and chronic (n=4 at 58-265 days) time points. Age- and region-matched non-ICH control tissues were obtained from patients who died of cardiological disease (n=3, age 63-79). After death, brain tissue was processed into formalin-fixed paraffin embedded tissue blocks, which were sectioned at 5 µm thickness using a microtome and mounted into Superfrost glass slides for immunohistochemical analysis.

Animals

Mice were housed under controlled conditions (temperature 21 ± 2°C, humidity 55 ± 10%, 12 h light/dark cycle) with ad libitum access to standard rodent chow and water. Ch25h-deficient mice (*Ch25h*$^{-/-}$) on a C57BL/6J background[23] were maintained and bred in-house to generate homozygous *Ch25h*$^{-/-}$ and *Ch25h*$^{+/+}$ littermate controls. Both male and female mice were used at 10–18 weeks of age. All animal experiments were carried out under the authority of a UK Home Office Project Licence (PPL: PP9466981) and approved by the University of Manchester Animal Welfare and Ethical Review Body. All reporting of animal experiments complied with the ARRIVE guidelines (Animal Research: Reporting in In Vivo Experiments[55]).

Collagenase model of intracerebral haemorrhage

ICH was induced using the collagenase-induced model[56]. Briefly, mice were anaesthetised using 1.5-2.0% isoflurane (in 30% O_2:70% N_2O) and core body temperature was maintained at 37 °C. Prior to any surgical steps, buprenorphine was administered (subcutaneous injection; 0.05 mg/kg), and the surgical area was shaved and treated with iodine. Animals were then secured in a stereotaxic frame and collagenase (bacterial type VII; 0.04 U in 0.5 µl sterile saline) was stereotaxically injected (at 1 µl min^{-1}) through a glass capillary pipette into the right striatum (0.0mm anterior/posterior, -2.0 mm lateral and -3.0mm deep from the dura). The pipette was retracted after 10 min and the wound sutured, before saline (1 ml per 100mg, subcutaneous) administration. Animals were allowed to recover from anaesthesia in a 24 °C thermostat cabinet and then given free access to mashed food and water under normal housing conditions.

Animals were randomly allocated to surgery days, and genotypes and drug treatments were blinded by an independent experimenter. All ICH surgery and subsequent behavioural tests were therefore performed blinded to genotype and treatment, and behavioural and histological analyses were performed blinded to genotype, treatment and sex. Genotype/treatment allocation was only revealed when all analyses were fully complete.

25HC *in vivo* treatment

25HC (Sigma-Aldrich) was prepared at a concentration of 3 mg ml^{-1} in hydroxypropyl-β-cyclodextrin (Cayman Chemical), which was dissolved in sterile saline at 37 g ml^{-1} and used as vehicle. Mice received intraperitoneal injections of 25HC (50 mg kg^{-1}) or vehicle control (0.45 g kg^{-1}) as previously reported[57,58], immediately following induction of ICH and subsequently once daily (for two days) after completion of behavioural testing.

Functional outcome measures

Animals were acclimated to testing rooms for at least 1 h before testing, which was performed in the same environment throughout. For all tests, a baseline (day 0) measurement was taken the day before

surgery and then repeated after ICH (days 1, 3 and 7 depending on the experiment). Body weight change was also assessed.

Modified neurological severity score: Neurobehavioral changes were assessed in an open cage using a 32-point neurological severity score (mNSS or neuroscore).

Cylinder test: Mice were placed into a glass cylinder (20 cm in diameter and 40 cm in height) and their activity was recorded for 10 min. The number of rears initiated with the left, right or both forepaws was quantified. Use of the impaired limb (%) was calculated relative to baseline.

Nest building: Nest-building behaviour was assessed by housing mice individually in clean cages containing 20 g nesting material mixed with wood shavings for 12 h overnight. Nest structure and height were assessed visually and scored on a 0-5 scale.

Grip strength: Forelimb grip strength was measured using a BIOSEB Grip Meter. Three measurements were obtained per animal and averaged. Values were expressed as percentage change relative to baseline.

Tissue preparation and histology

Under anaesthesia (3% isoflurane), mice were perfused transcardially with phosphate-buffered saline (PBS) followed by 4% paraformaldehyde (PFA). Brains were removed and post-fixed in 4% PFA solution and 24 h later transferred to a 30% sucrose solution for a further 24 h at 4°C. The brains were then embedded in optimal cutting temperature compound, snap-frozen in −50 °C isopentane, and stored at −70 °C until further processing. Coronal sections (10 µm) were cut using a Leica CM3050 cryostat and stored at −20 °C. Haematoma volume was assessed using haematoxylin and eosin staining. Ferric iron was visualised using Prussian blue staining (2% potassium ferricyanide and 2% hydrochloric acid; Abcam).

Immunostaining

To detect Ch25h, immunohistochemistry was performed on mouse and human brain sections. Human sections were deparaffinised in xylene, rehydrated through graded ethanol, and subjected to antigen retrieval (97.5 °C, Tris-EDTA buffer, pH 9.0). Sections were blocked with 5% normal goat serum (NGS) and incubated overnight at 4 °C with rabbit anti-Ch25h antibody (1:200, Aviva Systems Biology). Slides were incubated with biotinylated anti-rabbit secondary antibody (1:400), followed by ABC-alkaline phosphatase (AP) reagent and developed using AP substrate. Sections were counterstained with haematoxylin and mounted using DPX.

For Ch25h co-localisation, immunofluorescence was performed using a Tyramide SuperBoost Kit (Alexa Fluor 555). After antigen retrieval and blocking, sections were incubated with rabbit anti-Ch25h (1:200) followed by biotinylated secondary antibody and streptavidin-HRP. Tyramide signal amplification was performed for 7 min. A second antigen retrieval step was performed before Iba1 staining (1:500, Abcam)

and Alexa Fluor secondary antibody (1:400, Invitrogen). Slides were mounted using ProLong mounting medium. For BBB integrity, endogenous peroxidase activity was quenched using 0.3% H_2O_2, followed by blocking with 2% NGS and incubation with biotinylated goat anti-mouse IgG (1:200). Detection was performed using ABC-HRP and DAB substrate.

Brain image analysis

Images were collected using SlideViewer software v2.2 (3D-Histech Pannoramic-250 Flash Side Scanner using a 20x/ 0.80 Plan Apochromat objective (Zeiss) with specific filter sets for any fluorophore used). The haemorrhage area was measured (using CaseViewer) on sections and volume was calculated using area under the curve (using Prism). The intensity (integrated) of the iron stain was calculated in three peri-haematomal regions (3 sections/brain) using colour deconvolution with analysis performed on the FastBlue channel (Fiji software). For analysis of BBB breakdown, IgG integrated density was calculated (using Qupath) on 3 sections across the extent of the haematoma using colour deconvolution (channel set to DAB). All image analysis was carried out blind to the experimental group and quantification parameters were constant for the whole set of images for each marker. For Ch25h, the positive cell area was calculated on 3 perihaematomal regions (3 sections/brain) from the ipsilateral hemisphere and corresponding regions in the contralateral hemisphere, using FastRed channel after colour deconvolution (Fiji software).

Cell culture

Cells were cultured at 37 °C and 5% CO_2. BV2 microglia were maintained in RPMI-1640 supplemented with 10% FBS (foetal bovine serum) and PenStrep (100 units ml^{-1} penicillin and 100 µg ml^{-1} streptomycin) and passaged at full confluency using Trypsin-EDTA (up to passage 20). BV2 cells were seeded at 32,000 cells cm^{-2}. Primary BMDMs were generated from femoral bone marrow following red blood cell lysis. Cells were cultured for 7-8 days in DMEM with 10% FBS and PenStrep, supplemented with 30% L929-conditioned medium. BMDMs were seeded at 187,000 cells cm^{-2} in DMEM with 10% FBS and PenStrep.

Cells were treated with 100 µM haemin and 1 µM 25HC, 16 h after seeding for qPCR assays or 1-2 h after seeding for phagocytosis assays. Ethanol was used as a vehicle at matched concentrations.

RBC preparation

RBCs were prepared as previously described[59]. Blood was collected by cardiac puncture and separated using a 65%/35% Percoll gradient. RBCs were labelled with 50 µM pHrodo-SE and opsonised using rabbit anti-mouse RBC antibody (1 µg ml^{-1}). Oxidised RBCs were generated using 0.2 mM $CuSO_4$ and 5 mM L-ascorbic acid[60], washed in EDTA-containing PBS, and labelled with pHrodo-SE. RBCs were added at 1.87 × 10^6 cells cm^{-2} (based on a 1:10 ratio for BMDM:RBC) and centrifuged briefly (500 g, 5 s) to promote contact with phagocytes.

Live cell imaging

Before phagocytosis imaging, negative controls were incubated with 10 μM cytochalasin D for 30 min and then incubated again after RBCs were added. Imaging was performed using an Incucyte S3 (Essenbio) microscope or an Eclipse Ti inverted microscope (Nikon), both equipped with a humidified incubator maintaining 37°C and 5% CO_2. Point visiting was used to image multiple positions within the same time-course, and three positions per well were acquired at 20x magnification every hour for 10 h. pHrodo signal was analysed using Incucyte or ImageJ software. Area under the curve analyses were performed in GraphPad Prism software.

Cell density and cell death assays

Incucyte S3 (Essenbio) microscope or Eclipse Ti inverted microscopes (Nikon) microscopes and software were used as previously stated for cell death, density and area imaging. Cells were incubated with 0.5 μM Yo-Pro-1 (Invitrogen), and Yo-Pro-1-positive cells (dead cells) and confluency were imaged. Cells were then incubated with lysis solution (Promega, G1780) to capture an image of 100% Yo-Pro-1-positive cells (cell density), which was also used to expressed cell death as a percentage normalized to the total cell lysis control.

Cell death was also measured by assessing lactate dehydrogenase (LDH) release into cell culture supernatants, using the CytoTox 96 Non-Radioactive Cytotoxicity Assay (Promega, G1780) according to the manufacturer's instructions. Samples were quantified by reading absorbance at 490 nm in a Synergy HT microplate reader (Biotek Instruments). LDH release was expressed as a percentage normalized to a total cell lysis control.

qPCR

Mice were transcardially perfused with PBS, their brains were removed and a 4mm cube of brain tissue containing the haemorrhage or the contralateral region were dissected. Total RNA was isolated from the brain using TRIzol lysis buffer and a QIAGEN RNeasy® lipid tissue mini kit, according to the manufacturer’s instructions. RNA from cells was isolated using a standard TRIzol procedure or RNAEasy mini kit. qPCR was performed using Power SYBR Green Mastermix on StepOne Plus or QuantStudio 12 Flex systems. Gene expression was normalised using geometric averaging of *Hprt1/Rn18s* or *Hprt1/Gapdh*. Relative expression was calculated using the $2^{-\Delta\Delta CT}$ method and expressed as $\log_2$ fold change. Primer sequences are listed in Table S13.

Protein-ligand interaction analysis

The crystal structure of human LXRα in complex with a tert-butyl benzoate analogue (PDB ID: 5AVL) was retrieved from the Protein Data Bank. The receptor structure was pre-processed using AutoDock Tools (v1.5.6) by removing water molecules and co-crystallised ligands, adding polar hydrogens, and assigning Kollman charges. The docking search space was defined based on the ligand binding site and high-

scoring pockets predicted using p2rank. Grid centre coordinates were set to (x, y, z) = (75.7873, −5.7677, 16.4636). Molecular docking was performed using AutoDock Vina (v1.1.2), and binding poses were ranked according to predicted binding affinity. The lowest-energy pose was selected for further analysis. Protein-ligand interactions were characterised using the Protein-Ligand Interaction Profiler, and interaction diagrams were rendered using PyMOL (v2.5.0).

Single-cell RNA sequencing and analysis

Brains from male mice were perfused with PBS, and a 4-mm tissue block containing the haemorrhage core or contralateral region was dissected and snap-frozen in isopentane. Fixed tissue was processed using the Chromium Fixed RNA Profiling workflow with the Mouse Transcriptome Probe Set (10x Genomics) according to the manufacturer's instructions, and myelin was removed using a sucrose cushion[61]. Single-cell libraries were generated using a Chromium X controller and sequenced on an Illumina NovaSeq 6000 platform (paired-end 28 bp and 90 bp).

Raw sequencing data were processed using Cell Ranger (v8.0.0; 10x Genomics) and aligned to the mm10-2020-A mouse reference genome and Chromium Mouse Transcriptome Probe Set v1.0.1. Downstream analysis was performed in R (v4.4.3) using Bioconductor. Low-quality cells were identified using a combination of median absolute deviation and exact thresholds and removed prior to data integration. Doublet scores were inferred using scDblFinder. Batch correction was performed with mutual nearest neighbours (MNN) method (batchelor). The MNN-corrected matrix was used to create UMAP and t-SNE embeddings, and clustering was performed using Leiden and Louvain algorithms. Clusters were annotated using established marker genes, and doublet-enriched clusters were manually excluded. Differential expression analysis was performed on pseudobulked data using DESeq2, with false discovery rate (FDR) < 0.05 considered significant.

KEGG pathway enrichment was performed using over-representation analysis (ORA) and gene set enrichment analysis (GSEA). For ORA, genes with FDR < 0.05 and absolute $\log_2$ fold change ($\log_2$FC) > 1 were selected and analysed using ShinyGO (v0.85), using as background all expressed genes with baseMean > 1 and valid FDR estimates. For GSEA, genes were ranked using SIGN($\log_2$FC) x -log10(P-value), converted from ENSEMBL to Entrez identifiers, and analysed using the clusterProfiler framework. Single-cell pathway activity was quantified using AUCell based on literature-derived microglial gene programmes or KEGG pathways.

Bulk RNA sequencing and analysis

BMDMs were treated with 25HC and opsonised RBCs as previously stated, and total RNA was extracted using the RNeasy Mini Kit (Qiagen). RNA integrity was assessed using a 4200 TapeStation (Agilent). Libraries were prepared using the Illumina Stranded mRNA Prep Ligation Kit and sequenced on an Illumina NovaSeq 6000 platform (paired-end 59 bp). Reads were quality assessed using FastQC and FastQ Screen, trimmed using BBDuk, and aligned to the mouse reference genome (GRCm39) and gene annotation from Gencode (vM38) using STAR. Gene-level counts produced by using STAR was used to

perform differential expression analysis using DESeq2, including an interaction term to test for differential effects between 25HC treatment and RBC exposure. Genes with FDR < 0.05 were considered differentially expressed.

Over-representation analysis (ORA) of Gene Ontology biological process terms and KEGG pathways was performed using clusterProfiler. ORA was conducted separately for genes significantly regulated in opposite directions by 25HC treatment and RBC exposure (FDR < 0.05, based on the direction of log2 fold change), and for genes showing a significant treatment interaction effect (FDR < 0.05). All enrichment analyses used the full set of tested genes as the background universe.

Lipid droplet imaging

BMDMs were seeded on glass coverslips and treated with 25HC and opsonised RBCs as previously stated. Non internalised RBCs were washed twice with calcium-containing PBS, and BMDMs were fixed with PFA 4% in PBS. Cells were incubated with 5% BSA in PBST (PBS + 0.1% Tween-20) and a standard immunohistochemical protocol was performed then with anti-Iba1 antibody (1:500, Abcam) and anti-rabbit secondary antibody (1:500, Alexa Fluor 488®, Invitrogen). Cells were then incubated with LipidSpot 611 (1:2000, Biotium) and DAPI (1 μg ml^{-1}) for 10 min in PBS, air-dried and mounted in Prolong.

Images were collected blinded to treatment, on a Leica TCS SP8 AOBS upright confocal using a 63x objective. The confocal software was used to determine the optimal number of Z sections for 3D optical stacks and to process maximum intensity projections. Five fields of view were collected per biological sample. Using ImageJ, images were analysed for background removal and manually processed, blinded to treatment, to eliminate extracellular debris. LipidSpot area was analysed in ImageJ, and normalised to cell number, quantified as DAPI counts.

Statistical analysis

Statistical analyses were conducted using GraphPad Prism v10.2.2 (GraphPad). For behavioural analysis, G*Power software (v3.1.9.6) was used to calculate sample sizes using $\alpha = 0.05$, power ($1 - \beta = 0.8$) and an expected effect size of 20–25%, depending on the experiment. Shapiro-Wilk normality tests were used to identify parametric and non-parametric datasets. Parametric data are presented as mean ± standard error of the mean (SEM) and non-parametric and ordinal data as median ± interquartile range (IQR). To compare two independent datasets, the unpaired t-test (parametric test) or the Mann-Whitney test (non-parametric test) was chosen. To compare matched datasets, the paired two-tailed t-test was chosen. Kruskal-Wallis was used to compare non-repeated non-parametric measures of a single factor. Two-factor data were analysed by two-way ANOVA (no missing values) or mixed effects analysis (with missing values). Repeated measures two-way ANOVA was used for multiple time points. Residual distributions of two-way ANOVA tests were assessed using Q-Q plots and showed no major deviations from normality. Post hoc statistical tests are indicated in the corresponding figure legends. The variable *n* denotes the number of replicates, which were considered as individual human samples, individual

mouse, primary cells from individual mouse, cell passages from immortalised cells, or field of views in the LipidSpot assay. Significance was taken at $P < 0.05$.

Declarations

Acknowledgements

We would like to thank the Biological Services Facility at the University of Manchester for expert animal husbandry, the Bioimaging Core Facility at the University of Manchester for their help with imaging and the University of Manchester Genomic Technologies and Bioinformatics Core Facilities for their assistance with single-cell and bulk RNA-Sequencing. We also want to acknowledge the Edinburgh Brain Bank for the supply of human tissue.

Funding

This work was supported by a Medical Research Council grant (MR/Y004183/1) and the University of Manchester-China Scholarship Council joint scholarship. PRK was supported by a Medical Research Council New Investigator grant (MR/T03291X/1). AB was supported by a 4-year British Heart Foundation PhD award (FS/4yPhD/F/22/34179) at the University of Manchester.

Data Availability

Bulk and single-cell RNA-seq data have been deposited in the ArrayExpress database at EMBL-EBI under accession number E-MTAB-16464 and E-MTAB-16495 respectively.

Competing Interests

There are no financial or non-financial interests that are directly or indirectly related to this work.

Ethical approval

The use of human post-mortem brain tissue was obtained from the Edinburgh Brain Bank, use was approved by the East of Scotland Research Ethics Service REC 1 (REC reference 21/ES/0084), in accordance with the Declaration of Helsinki principles. This study involved the use of donated post-mortem tissue and did not involve research conducted directly with human participants. All scientific procedures using animals were performed in accordance with the Animals (Scientific Procedures) Act 1986 under relevant UK Home Office licences and approved by the local Animal Welfare and Ethical Review Board (University of Manchester, UK).

Author Contributions

Conceptualization: R.Z., V.S.T., S.C., P.R.K. and C.B.L.; Formal analysis: R.Z., V.S.T., I-H.L. and C.B.L.; Investigation: R.Z., V.S.T., A.B., R.G., M.E., Z.D. and S.C.; Resources: C.P., S.M.A., P.R.K. and C.B.L.; Data Curation: R.Z., V.S.T, C.B.L.; Visualization: V.S.T, P.R.K. and C.B.L; Supervision: V.S.T., P.R.K. and C.B.L.;

Writing - Original Draft: V.S.T., P.R.K. and C.B.L; Writing - Editing: R.Z., V.S.T., A.B., I-H.L., S.M.A, P.R.K. and C.B.L.

References

1. Parry-Jones, A. R. *et al.* World Stroke Organization (WSO): Global intracerebral hemorrhage factsheet 2025. *Int J Stroke* **20**, 145-150 (2025). https://doi.org:10.1177/17474930241307876
2. Liu, J., Zhu, Z. & Leung, G. K. Erythrophagocytosis by Microglia/Macrophage in Intracerebral Hemorrhage: From Mechanisms to Translation. *Front Cell Neurosci* **16**, 818602 (2022). https://doi.org:10.3389/fncel.2022.818602
3. Hanley, D. F. *et al.* Efficacy and safety of minimally invasive surgery with thrombolysis in intracerebral haemorrhage evacuation (MISTIE III): a randomised, controlled, open-label, blinded endpoint phase 3 trial. *Lancet* **393**, 1021-1032 (2019). https://doi.org:10.1016/S0140-6736(19)30195-3
4. Wang, G., Wang, L., Sun, X. G. & Tang, J. Haematoma scavenging in intracerebral haemorrhage: from mechanisms to the clinic. *J Cell Mol Med* **22**, 768-777 (2018). https://doi.org:10.1111/jcmm.13441
5. Chang, C. F. *et al.* Alternative activation-skewed microglia/macrophages promote hematoma resolution in experimental intracerebral hemorrhage. *Neurobiol Dis* **103**, 54-69 (2017). https://doi.org:10.1016/j.nbd.2017.03.016
6. Chang, C. F. *et al.* Erythrocyte efferocytosis modulates macrophages towards recovery after intracerebral hemorrhage. *J Clin Invest* **128**, 607-624 (2018). https://doi.org:10.1172/JCI95612
7. Chang, C. F. *et al.* Divergent Functions of Tissue-Resident and Blood-Derived Macrophages in the Hemorrhagic Brain. *Stroke* **52**, 1798-1808 (2021). https://doi.org:10.1161/STROKEAHA.120.032196
8. Li, Z. *et al.* Kruppel-Like Factor 4 Regulation of Cholesterol-25-Hydroxylase and Liver X Receptor Mitigates Atherosclerosis Susceptibility. *Circulation* **136**, 1315-1330 (2017). https://doi.org:10.1161/CIRCULATIONAHA.117.027462
9. Bottemanne, P. *et al.* 25-Hydroxycholesterol metabolism is altered by lung inflammation, and its local administration modulates lung inflammation in mice. *FASEB J* **35**, e21514 (2021). https://doi.org:10.1096/fj.202002555R
10. Reboldi, A. *et al.* Inflammation. 25-Hydroxycholesterol suppresses interleukin-1-driven inflammation downstream of type I interferon. *Science* **345**, 679-684 (2014). https://doi.org:10.1126/science.1254790
11. Van Hove, H. *et al.* A single-cell atlas of mouse brain macrophages reveals unique transcriptional identities shaped by ontogeny and tissue environment. *Nat Neurosci* **22**, 1021-1035 (2019). https://doi.org:10.1038/s41593-019-0393-4
12. Chen, M. B. *et al.* Brain Endothelial Cells Are Exquisite Sensors of Age-Related Circulatory Cues. *Cell Rep* **30**, 4418-4432 e4414 (2020). https://doi.org:10.1016/j.celrep.2020.03.012

13. Jeong, H. W. *et al.* Single-cell transcriptomics reveals functionally specialized vascular endothelium in brain. *Elife* **11** (2022). https://doi.org:10.7554/eLife.57520
14. Toral-Rios, D. *et al.* Cholesterol 25-hydroxylase mediates neuroinflammation and neurodegeneration in a mouse model of tauopathy. *J Exp Med* **221** (2024). https://doi.org:10.1084/jem.20232000
15. Wong, M. Y. *et al.* 25-Hydroxycholesterol amplifies microglial IL-1beta production in an apoE isoform-dependent manner. *J Neuroinflammation* **17**, 192 (2020). https://doi.org:10.1186/s12974-020-01869-3
16. Czapski, G. A., Zhao, Y., Lukiw, W. J. & Strosznajder, J. B. Acute Systemic Inflammatory Response Alters Transcription Profile of Genes Related to Immune Response and Ca(2+) Homeostasis in Hippocampus; Relevance to Neurodegenerative Disorders. *Int J Mol Sci* **21** (2020). https://doi.org:10.3390/ijms21217838
17. Jang, J. *et al.* 25-hydroxycholesterol contributes to cerebral inflammation of X-linked adrenoleukodystrophy through activation of the NLRP3 inflammasome. *Nat Commun* **7**, 13129 (2016). https://doi.org:10.1038/ncomms13129
18. Ruiz, F. *et al.* Endothelial cell-derived oxysterol ablation attenuates experimental autoimmune encephalomyelitis. *EMBO reports* (2023). https://doi.org:10.15252/embr.202255328
19. Zhang, Y. *et al.* Novel CH25H(+) and OASL(+) microglia subclusters play distinct roles in cerebral ischemic stroke. *J Neuroinflammation* **20**, 115 (2023). https://doi.org:10.1186/s12974-023-02799-6
20. Lin, F. *et al.* 25-Hydroxycholesterol protecting from cerebral ischemia-reperfusion injury through the inhibition of STING activity. *Aging (Albany NY)* **13**, 20149-20163 (2021). https://doi.org:10.18632/aging.203337
21. Tuong, Z. K. *et al.* Disruption of Roralpha1 and cholesterol 25-hydroxylase expression attenuates phagocytosis in male Roralphasg/sg mice. *Endocrinology* **154**, 140-149 (2013). https://doi.org:10.1210/en.2012-1889
22. Madenspacher, J. H. *et al.* Cholesterol 25-hydroxylase promotes efferocytosis and resolution of lung inflammation. *JCI Insight* **5** (2020). https://doi.org:10.1172/jci.insight.137189
23. Wyss, A. *et al.* The EBI2-oxysterol axis promotes the development of intestinal lymphoid structures and colitis. *Mucosal Immunol* **12**, 733-745 (2019). https://doi.org:10.1038/s41385-019-0140-x
24. Janowski, B. A. *et al.* Structural requirements of ligands for the oxysterol liver X receptors LXRalpha and LXRbeta. *Proc Natl Acad Sci U S A* **96**, 266-271 (1999). https://doi.org:10.1073/pnas.96.1.266
25. Williams, S. *et al.* X-ray crystal structure of the liver X receptor beta ligand binding domain: regulation by a histidine-tryptophan switch. *J Biol Chem* **278**, 27138-27143 (2003). https://doi.org:10.1074/jbc.M302260200
26. Matsui, Y. *et al.* Discovery and structure-guided optimization of tert-butyl 6-(phenoxymethyl)-3-(trifluoromethyl)benzoates as liver X receptor agonists. *Bioorg Med Chem Lett* **25**, 3914-3920 (2015). https://doi.org:10.1016/j.bmcl.2015.07.047
27. Yan, R. *et al.* A structure of human Scap bound to Insig-2 suggests how their interaction is regulated by sterols. *Science* **371** (2021). https://doi.org:10.1126/science.abb2224

28. Heisler, D. B. *et al.* A concerted mechanism involving ACAT and SREBPs by which oxysterols deplete accessible cholesterol to restrict microbial infection. *eLife* **12:e83534** (2023). https://doi.org:10.7554/eLife.83534
29. Hammond, T. R. *et al.* Single-Cell RNA Sequencing of Microglia throughout the Mouse Lifespan and in the Injured Brain Reveals Complex Cell-State Changes. *Immunity* **50**, 253-271 e256 (2019). https://doi.org:10.1016/j.immuni.2018.11.004
30. Keren-Shaul, H. *et al.* A Unique Microglia Type Associated with Restricting Development of Alzheimer's Disease. *Cell* **169**, 1276-1290 e1217 (2017). https://doi.org:10.1016/j.cell.2017.05.018
31. Epstein, C. E., Elidemir, O., Colasurdo, G. N. & Fan, L. L. Time course of hemosiderin production by alveolar macrophages in a murine model. *Chest* **120**, 2013-2020 (2001). https://doi.org:10.1378/chest.120.6.2013
32. Liu, S. *et al.* Comparative analysis of H&E and Prussian blue staining in a mouse model of cerebral microbleeds. *J Histochem Cytochem* **62**, 767-773 (2014). https://doi.org:10.1369/0022155414546692
33. Kovtunovych, G., Eckhaus, M. A., Ghosh, M. C., Ollivierre-Wilson, H. & Rouault, T. A. Dysfunction of the heme recycling system in heme oxygenase 1-deficient mice: effects on macrophage viability and tissue iron distribution. *Blood* **116**, 6054-6062 (2010). https://doi.org:10.1182/blood-2010-03-272138
34. Li, Q. *et al.* Microglia-derived interleukin-10 accelerates post-intracerebral hemorrhage hematoma clearance by regulating CD36. *Brain Behav Immun* **94**, 437-457 (2021). https://doi.org:10.1016/j.bbi.2021.02.001
35. Deng, X. *et al.* Mas receptor activation facilitates innate hematoma resolution and neurological recovery after hemorrhagic stroke in mice. *J Neuroinflammation* **21**, 106 (2024). https://doi.org:10.1186/s12974-024-03105-8
36. Tuong, Z. K. *et al.* RORalpha and 25-Hydroxycholesterol Crosstalk Regulates Lipid Droplet Homeostasis in Macrophages. *PLoS One* **11**, e0147179 (2016). https://doi.org:10.1371/journal.pone.0147179
37. Marschallinger, J. *et al.* Lipid-droplet-accumulating microglia represent a dysfunctional and proinflammatory state in the aging brain. *Nat Neurosci* **23**, 194-208 (2020). https://doi.org:10.1038/s41593-019-0566-1
38. Zhao, Q. *et al.* Cholesterol metabolic reprogramming mediates microglia-induced chronic neuroinflammation and hinders neurorestoration following stroke. *Nat Metab* **7**, 2099-2116 (2025). https://doi.org:10.1038/s42255-025-01379-7
39. Arbaizar-Rovirosa, M. *et al.* Aged lipid-laden microglia display impaired responses to stroke. *EMBO Mol Med* **15**, e17175 (2023). https://doi.org:10.15252/emmm.202217175
40. Xiang, R. *et al.* Spatiotemporal transcriptomic maps of mouse intracerebral hemorrhage at single-cell resolution. *Neuron* **113**, 2102-2122 e2107 (2025). https://doi.org:10.1016/j.neuron.2025.04.026

41. Wu, Z., Zhao, Q., Hu, Z. & Jiao, D. Lipid droplets deposition in perihematoma tissue is associated with neurological dysfunction after intracerebral hemorrhage. *Neuroreport* **36**, 239-246 (2025). https://doi.org:10.1097/WNR.0000000000002136
42. Zhang, R. *et al.* Enhanced liver X receptor signalling reduces brain injury and promotes tissue regeneration following experimental intracerebral haemorrhage: roles of microglia/macrophages. *Stroke Vasc Neurol* **8**, 486-502 (2023). https://doi.org:10.1136/svn-2023-002331
43. Abrams, M. E. *et al.* Oxysterols provide innate immunity to bacterial infection by mobilizing cell surface accessible cholesterol. *Nat Microbiol* **5**, 929-942 (2020). https://doi.org:10.1038/s41564-020-0701-5
44. Cashikar, A. G. *et al.* Regulation of astrocyte lipid metabolism and ApoE secretion by the microglial oxysterol, 25-hydroxycholesterol. *J Lipid Res* **64**, 100350 (2023). https://doi.org:10.1016/j.jlr.2023.100350
45. Tapia, V. S. *et al.* The role of 25-hydroxycholesterol in the pathophysiology of brain vessel dysfunction associated with infection and cholesterol dysregulation. *Dis Model Mech* **18** (2025). https://doi.org:10.1242/dmm.052145
46. Trzeciak, A., Wang, Y. T. & Perry, J. S. A. First we eat, then we do everything else: The dynamic metabolic regulation of efferocytosis. *Cell Metab* **33**, 2126-2141 (2021). https://doi.org:10.1016/j.cmet.2021.08.001
47. Yin, C. & Heit, B. Cellular Responses to the Efferocytosis of Apoptotic Cells. *Front Immunol* **12**, 631714 (2021). https://doi.org:10.3389/fimmu.2021.631714
48. Kober, A. C. *et al.* Implications of cerebrovascular ATP-binding cassette transporter G1 (ABCG1) and apolipoprotein M in cholesterol transport at the blood-brain barrier. *Biochim Biophys Acta Mol Cell Biol Lipids* **1862**, 573-588 (2017). https://doi.org:10.1016/j.bbalip.2017.03.003
49. Do, T. M. *et al.* Direct evidence of abca1-mediated efflux of cholesterol at the mouse blood-brain barrier. *Mol Cell Biochem* **357**, 397-404 (2011). https://doi.org:10.1007/s11010-011-0910-6
50. Castoreno, A. B. *et al.* Transcriptional regulation of phagocytosis-induced membrane biogenesis by sterol regulatory element binding proteins. *Proc Natl Acad Sci U S A* **102**, 13129-13134 (2005). https://doi.org:10.1073/pnas.0506716102
51. Wang, S. *et al.* Cholesterol 25-Hydroxylase inhibits SARS-CoV-2 and other coronaviruses by depleting membrane cholesterol. *The EMBO Journal* **39** (2020). https://doi.org:10.15252/embj.2020106057
52. Xiao, J. *et al.* 25-Hydroxycholesterol regulates lysosome AMP kinase activation and metabolic reprogramming to educate immunosuppressive macrophages. *Immunity* **57**, 1087-1104 e1087 (2024). https://doi.org:10.1016/j.immuni.2024.03.021
53. Lancaster, C. E. *et al.* Phagosome resolution regenerates lysosomes and maintains the degradative capacity in phagocytes. *J Cell Biol* **220** (2021). https://doi.org:10.1083/jcb.202005072
54. Harvey, L. D. *et al.* Lysosomal dysfunction and inflammatory sterol metabolism in pulmonary arterial hypertension. *Science* **387**, eadn7277 (2025). https://doi.org:10.1126/science.adn7277

55. Kilkenny, C., Browne, W. J., Cuthill, I. C., Emerson, M. & Altman, D. G. Vol. 8 e1000412 (Public Library of Science, 2010).
56. Barrington, J. *et al.* Interleukin-1 regulates myeloid cell trafficking and cerebral blood flow following intracerebral haemorrhage. *Dis Model Mech* **18** (2025). https://doi.org:10.1242/dmm.052306
57. Madenspacher, J. H. *et al.* 25-hydroxycholesterol exacerbates vascular leak during acute lung injury. *JCI Insight* (2023). https://doi.org:10.1172/jci.insight.155448
58. Li, C. *et al.* 25-Hydroxycholesterol Protects Host against Zika Virus Infection and Its Associated Microcephaly in a Mouse Model. *Immunity* **46**, 446-456 (2017). https://doi.org:10.1016/j.immuni.2017.02.012
59. Cook, J. R. *et al.* LRRC8A is dispensable for a variety of microglial functions and response to acute stroke. *Glia* **70**, 1068-1083 (2022). https://doi.org:10.1002/glia.24156
60. Olsson, M. & Oldenborg, P. A. CD47 on experimentally senescent murine RBCs inhibits phagocytosis following Fcgamma receptor-mediated but not scavenger receptor-mediated recognition by macrophages. *Blood* **112**, 4259-4267 (2008). https://doi.org:10.1182/blood-2008-03-143008
61. Nott, A., Schlachetzki, J. C. M., Fixsen, B. R. & Glass, C. K. Nuclei isolation of multiple brain cell types for omics interrogation. *Nat Protoc* **16**, 1629-1646 (2021). https://doi.org:10.1038/s41596-020-00472-3

Figures

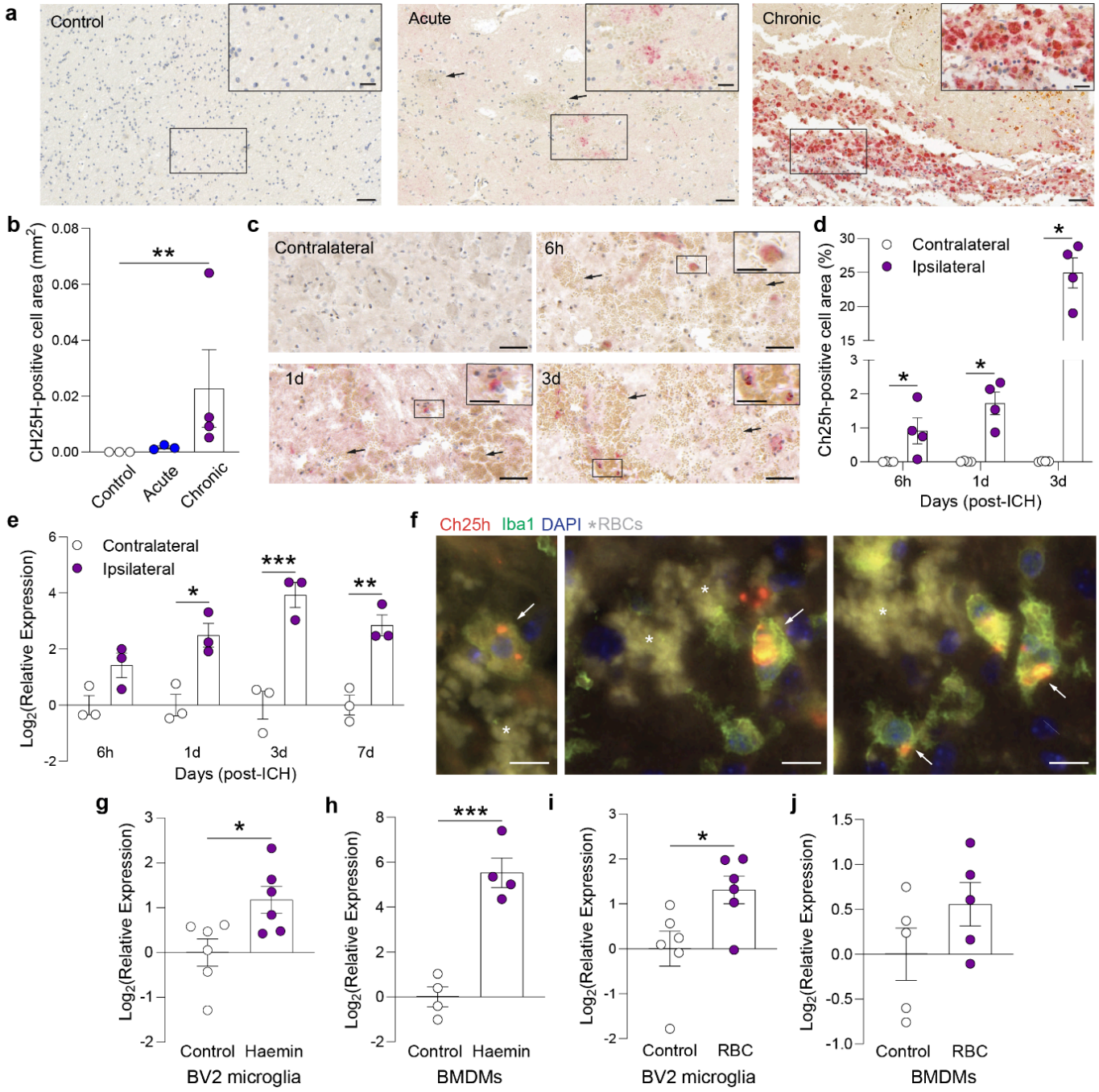

Figure 1

CH25H expression increases after intracerebral haemorrhage. a-b, Representative images (**a**) and quantification (**b**) of CH25H immunohistochemistry in control, acute and chronic intracerebral haemorrhage (ICH) human brain tissues (n=3-4 individuals per group). CH25H expression is observed in red, and black arrows indicate red blood cell (RBC) clusters. Scale bars = 50 µm (main panels) and 20 µm (inserts). **c-d**, Representative images (**c**) and quantification (**d**) of Ch25h immunohistochemistry in contralateral and ipsilateral mouse brain tissue (n=4 mice per group), 6 h to 3 days after collagenase-induced ICH. Ch25h expression is observed in red; black arrows indicate RBC clusters. Scale bars = 50 µm (main panels) and 20 µm (inserts). **e**, qPCR analysis of *Ch25h*expression (6 h to 7days post-ICH), with ipsilateral brain samples normalised to contralateral (n=3 mice per group). **f**, Representative images

of Ch25h (red) and Iba1 (green) immunofluorescence in mouse brain haematoma, 3 days after ICH. Arrows indicate Ch25H+ Iba1+ cells; asterisks indicate RBC autofluorescence. Scale bars = 10 μm. **g-j**, qPCR analysis of *Ch25h*expression in BV2 microglia (n=6 cell passages per group) (**g**, **i**) or bone-marrow derived macrophages (n=4-5 mice per group) (**h**, **j**), 6 h after haemin treatment (100 μM) (**g, h**) or phagocytosis of IgG-opsonised RBCs (**i, j**). Statistics were performed using a Kruskal–Wallis test compared to control (**b**), two-way ANOVA with Tukey's post hoc multiple comparisons (**d-e**) and unpaired *t*-test (**g-j**). Data are mean ± SEM. * P < 0.05; ** P < 0.01; *** P < 0.001.

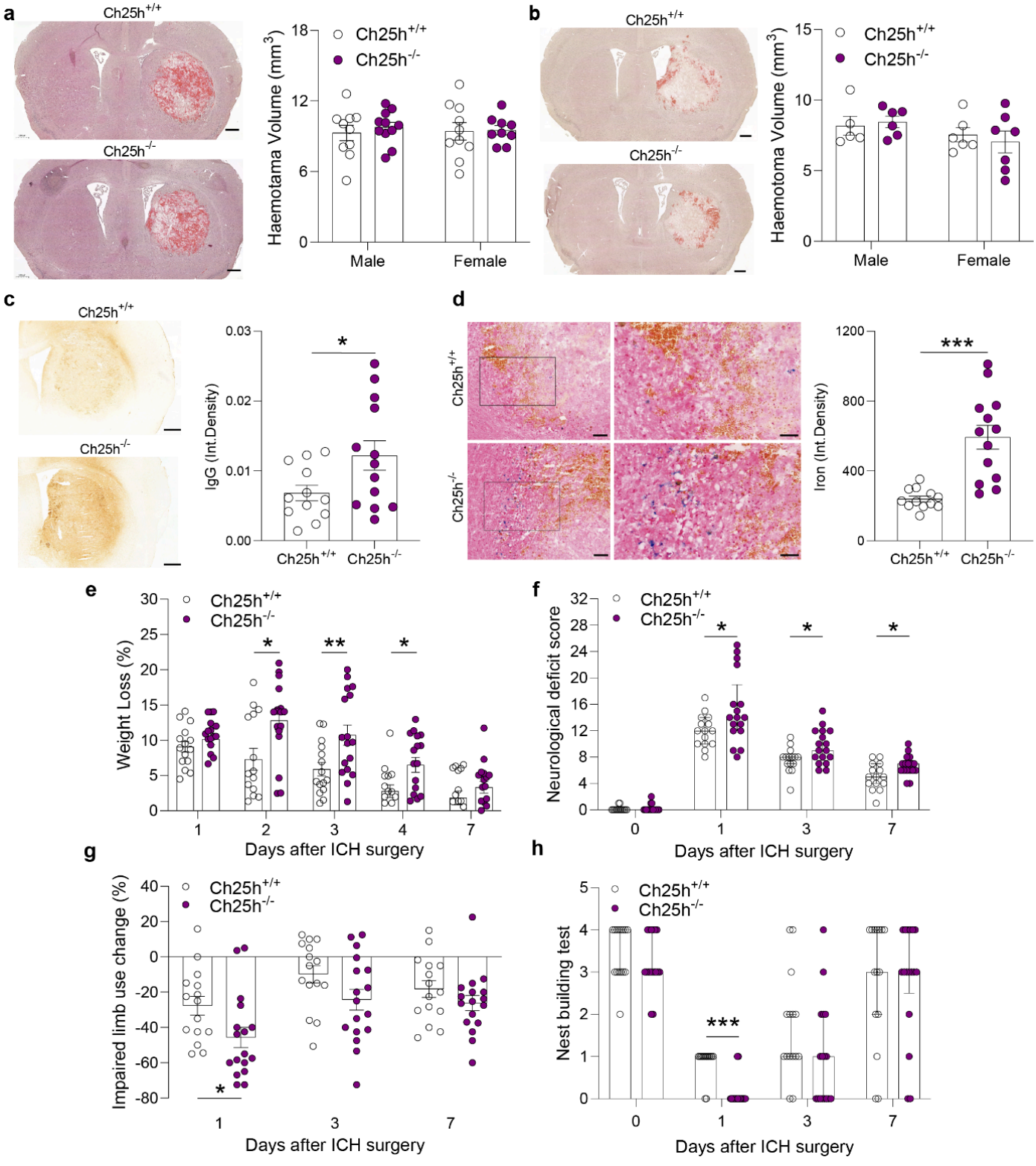

Figure 2

Ch25h deficiency leads to worse outcomes after ICH. a,b, Representative images (left) and quantification (right) of haematoma volume at 1 day (**a**) and 3 days (**b**) after ICH in male and female, *Ch25h*$^{+/+}$ and *Ch25h*$^{-/-}$ mice. (**a**) *Ch25h*$^{+/+}$: n= 10 males and 10 females; and *Ch25h*$^{-/-}$: n= 11 males and 9 females; (**b**) *Ch25h*$^{+/+}$: n= 5 males and 6 females; and *Ch25h*$^{-/-}$: n= 6 males and 7 females. Scale bar = 500 μm. **c,d**, Representative images (left) and quantification (right) of brain blood barrier (BBB) permeability measured by IgG staining (**c**) and iron deposition measured by Perls' Prussian Blue staining (**d**) 3 days after ICH in Ch25h$^{+/+}$ and Ch25h$^{-/-}$ mice (n=12-13 mice per group). Scale bar = 500 μm (**c**), 100 μm (main panels, **d**) and 50 μm (inserts, **d**). **e**, Longitudinal comparison of weight loss (**e**), neurological deficit score (**f**), impaired limb use in cylinder test (**g**) and nest building (**h**) from baseline to 7 days post-ICH, in Ch25h$^{+/+}$ and Ch25h$^{-/-}$ mice (n=15-17 mice per genotype). Statistics were performed using two-way ANOVA with Fisher's Least Significant Difference (LSD) post hoc multiple comparisons (**a-b**), unpaired *t*-test (**c-d**), and repeated measures two-way ANOVA with Tukey's post hoc multiple comparisons (**e-h**). Data are mean ± SEM (**a-e**, **g**) or median ± IQR (**f, h**). * P < 0.05; ** P < 0.01; *** P < 0.001.

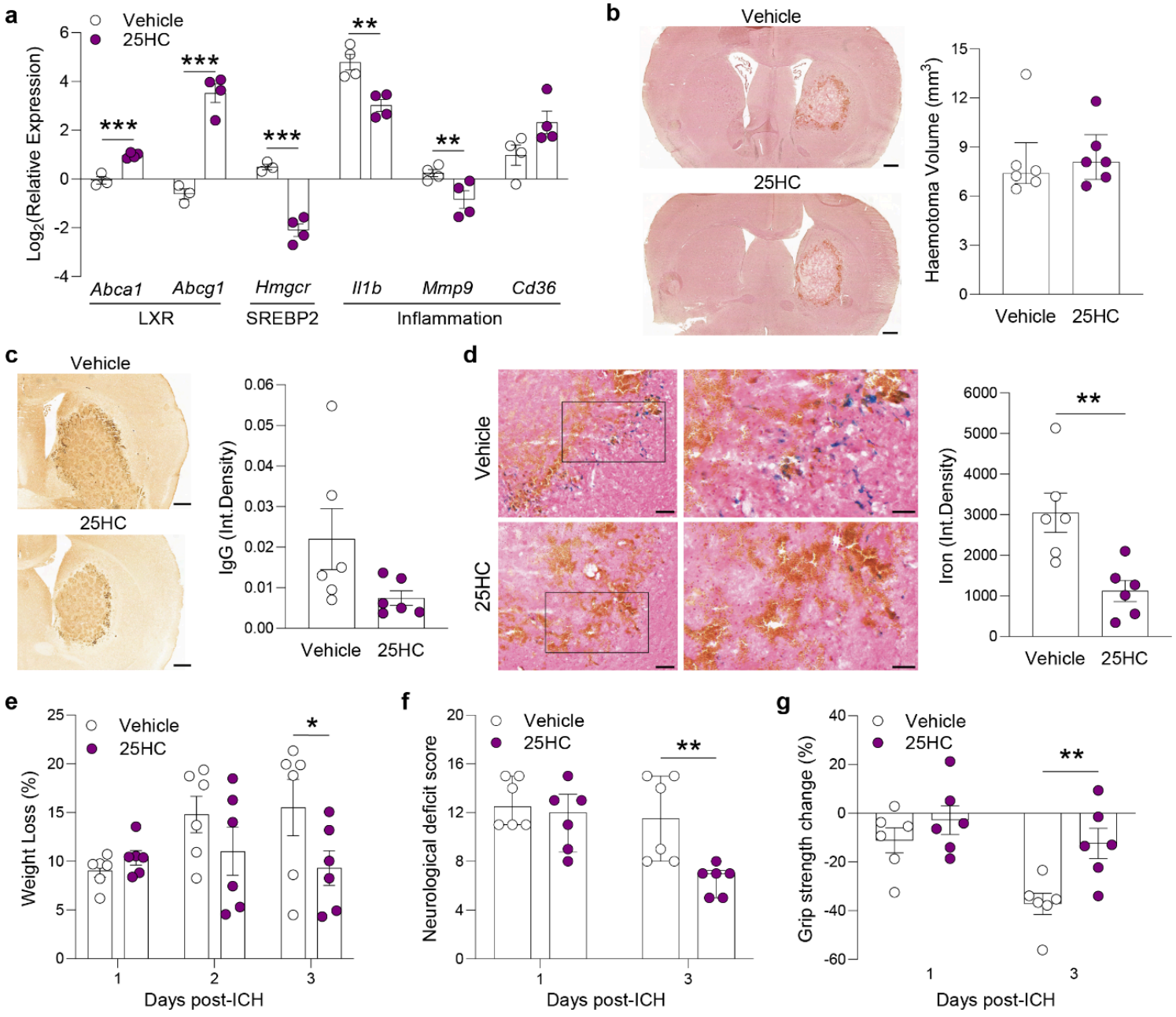

Figure 3

25HC treatment improves outcomes after ICH. a, Gene expression quantification by qPCR analysis in brain tissue from vehicle and 25HC-treated mice (50 mg kg^{-1}; n=3-4 mice per group), 1 day after ICH. Relative values for ipsilateral vs contralateral change are shown for each mouse. **b-d**, Representative images (left) and quantification (right) of haematoma volume (**b**), IgG staining (**c**) and Perls' Prussian Blue staining (**d**) 3 days after ICH in vehicle or 25HC-treated mice (n=6 mice per group). Scale bars = 500 µm (**b**, **c**), 100 µm (main panels, **d**) and 50 µm (inserts, **d**). **e**, Longitudinal comparison of weight loss (**e**), neurological deficit score (**f**), impaired limb use in cylinder test (**g**) and grip strength change (**g**) from baseline to 3 days post-ICH, in vehicle and 25HC-treated mice (n=6 mice per group). Statistics used the unpaired *t*-test (**a, c, d**), Mann–Whitney U test (**b**), repeated measures two-way ANOVA with Tukey's post

hoc multiple comparisons (**e**), or with Fisher's LSD post hoc multiple comparisons (**f, g**). Data are mean ± SEM (**a-e, g**) or median ± IQR (**b, f**). * P < 0.05; ** P < 0.01; *** P < 0.001.

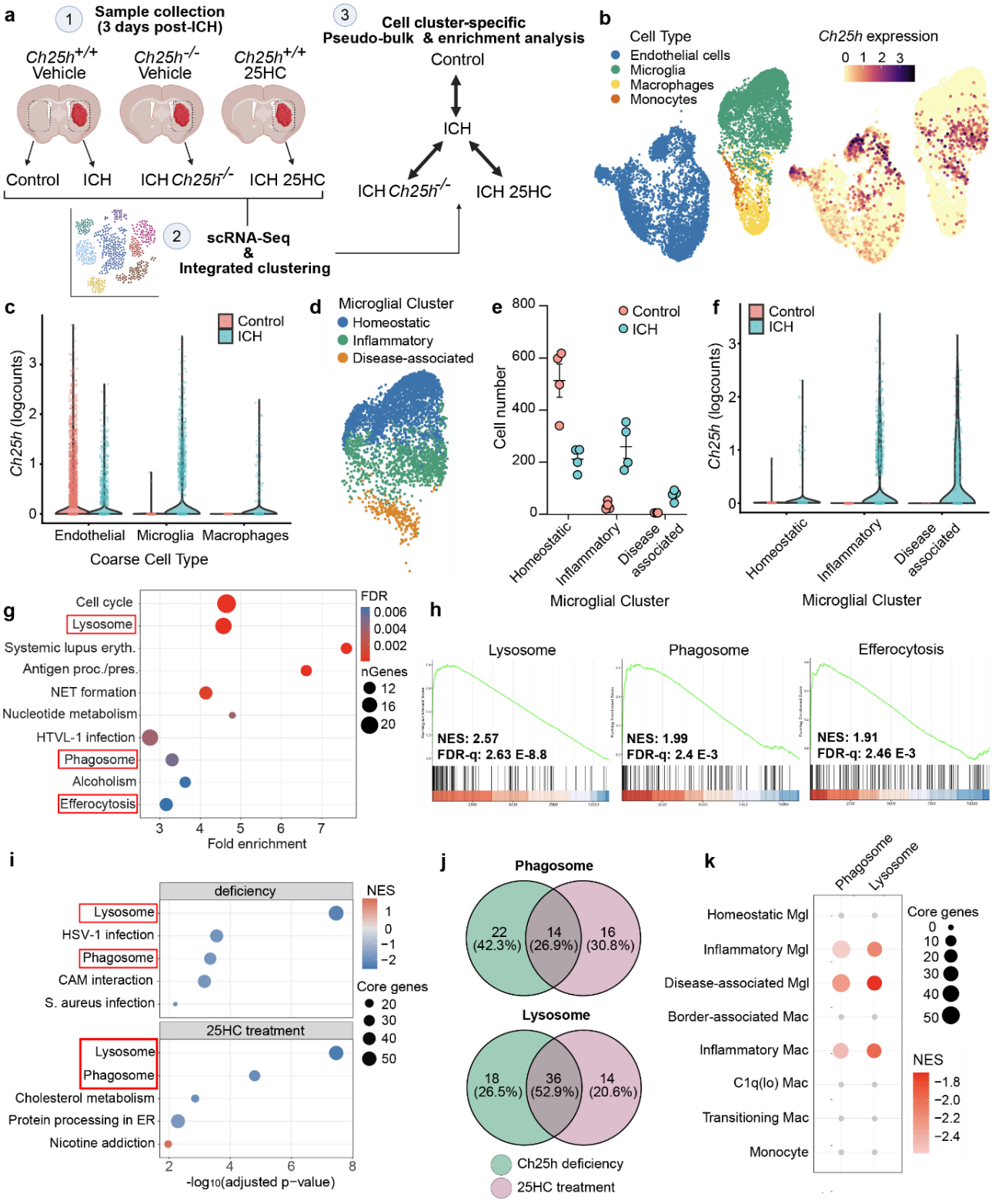

Figure 4

Ch25h expression is associated with a phagocytic microglial state after ICH and shapes phago-lysosomal gene programmes. a, Schematic of the single-cell RNA-seq experimental design. Mouse brain tissue was collected (dashed lines) 3 days after ICH from the contralateral (Control) and ICH hemispheres of *Ch25h*$^{+/+}$, *Ch25h*$^{-/-}$, and 25HC-treated *CH25h*$^{+/+}$ mice (n=4 male mice per group), followed by joint cell clustering and cluster-specific pseudo-bulk analysis. **b**, MNN-TSNE representations of endothelial-immune cell types in pooled control and ICH conditions, labelled by coarse cell type (left) and *Ch25h* expression (right). **c**, Violin plot showing *Ch25h* cell expression in endothelial, macrophage and microglial coarse cell types in control and ICH. **d**, MNN-TSNE representation of microglial clusters in pooled control and ICH conditions. **e**, Cell number of each microglia cluster in control and ICH samples (n=4 mice per group). Data are mean ± SEM. **f**, Violin plot showing *Ch25h* cell expression in microglial clusters in control and ICH. **g**, Top ten enriched KEGG pathways in over-representation analysis (ORA) of significantly upregulated genes from the control vs ICH comparison in inflammatory microglia. Dot colour indicates false discovery rate (FDR), and dot size represents the number of genes contributing to each pathway. **h**, Gene set enrichment analysis (GSEA) of the inflammatory microglia showing positive enrichment of lysosome, phagosome, and efferocytosis KEGG pathways from the control vs ICH comparison. Normalised enrichment score (NES) and FDR are indicated within each plot. **i**, Top five enriched KEGG pathways identified by GSEA in the inflammatory microglia for *Ch25h* deficiency (ICH vs ICH *Ch25h*$^{-/-}$) and 25HC treatment (ICH vs ICH 25HC) comparisons. Dot colour indicates NES, and dot size represents the number of genes contributing to each pathway. **j**, Venn diagram showing the number (and percentage) of genes driving lysosome and phagosome KEGG pathway enrichment by GSEA in **i**. **k**, GSEA of phagosome and lysosome KEGG pathways in 25HC treatment comparison across microglial (Mgl) and macrophage (Mac) clusters. Dot colour indicates NES, and dot size represents the number of genes contributing to each pathway.

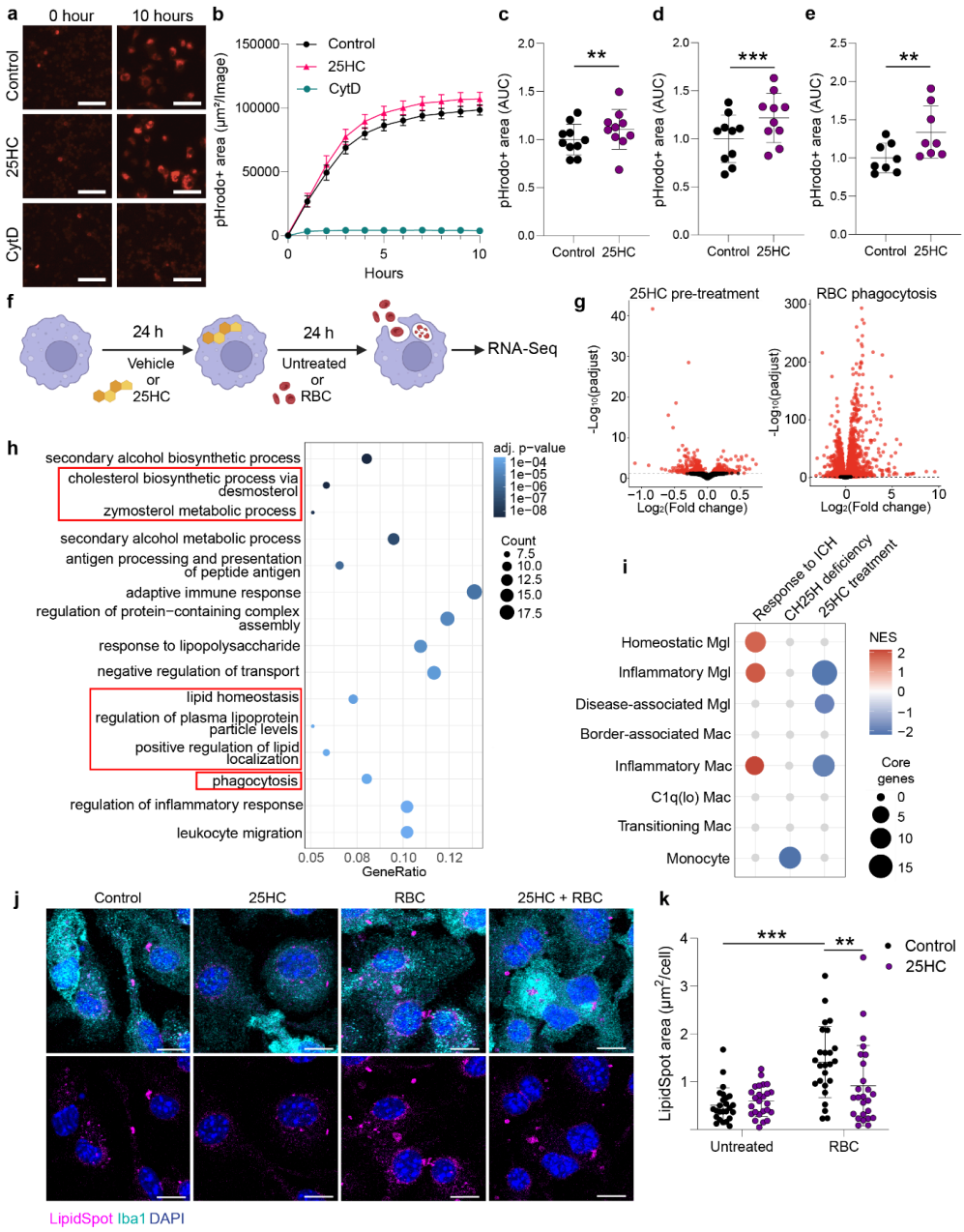

Figure 5

25HC promotes RBC phagocytosis and modulates lipid-handling pathways. a-c, pHrodo-based phagocytosis assay in bone marrow-derived macrophages (BMDMs) pre-treated with 25HC (1 µM, 24 h) and then exposed to pHrodo-labelled oxidised red blood cells (oxRBCs) (n=10 mice per group). Representative images of oxRBC uptake (**a**), time course (**b**), and area under the curve (AUC) analysis (**c**) are shown. Cytochalasin D 10 µM (CytD) was used as a phagocytosis inhibitor. Scale bars = 40 µm. **d-e**,

AUC analysis of pHrodo-labelled IgG-opsonised RBCs (opsoRBC) phagocytosis by BMDMs (n=10 mice per group) pre-treated with 25HC (**d**) or BV2 microglia (n=8 cell passages per group) pre-treated and co-treated during phagocytosis with 25HC (**e**). **f**, Experimental design for bulk RNA-seq of BMDMs following 25HC pre-treatment and RBC phagocytosis (n=4 mice per group). **g**, Volcano plots showing differential expression of genes in BMDMs in response to 25HC pre-treatment (right) or RBC phagocytosis (left). Red dots indicate genes with adjusted P-value < 0.05. **h**, Top fifteen enriched Gene Ontology (GO) Biological Process terms in ORA of genes that were significantly downregulated by 25HC pre-treatment and upregulated RBC phagocytosis. Dot colour indicates adj. P-value, and dot size represents the number of genes contributing to each term. **i**, GSEA of cholesterol metabolism KEGG pathway in response to ICH, CH25H deficiency and 25HC treatment comparisons across microglial (Mgl) and macrophage (Mac) clusters. Dot colour indicates NES, and dot size represents the number of genes contributing to the pathway. **j-k**, Lipid droplet analysis in BMDMs pre-treated with 25HC and then exposed to opsoRBC phagocytosis for 24h. Representative images of immunofluorescence (**j**) and quantification (n=25 field of views, from 5 mice) (**k**) are shown. LipidSpot is magenta, Iba1 is cyan and DAPI is blue. Scale bars = 10 μm. Statistics were performed using paired two-tailed *t*-test (**c-e**) or two-way ANOVA with Fisher's LSD post hoc multiple comparisons (**k**). Data are mean ± SEM. ** P < 0.01; *** P < 0.001.

Supplementary Files

This is a list of supplementary files associated with this preprint. Click to download.

- ZhouetalSupplementaryTables.xlsx
- ZhouetalSupplementaryFigures.docx